DISEASES AND DISORDERS

CXCL12/CXCR4-Rac1–mediated migration of osteogenic precursor cells contributes to pathological new bone formation in ankylosing spondylitis

Haowen Cui[1,2]†, Zihao Li[1,2]†, Siwen Chen[1,2]†, Xiang Li[1,2], Dongying Chen[3], Jianru Wang[1,2], Zemin Li[1,2], Wenjun Hao[1,2], Fangling Zhong[1,2], Kuibo Zhang[4], Zhaomin Zheng[1,2], Zhongping Zhan[3], Hui Liu[1,2]*

Ankylosing spondylitis (AS) is a chronic inflammatory disease characterized by inflammatory back pain and spinal ankylosis due to pathological new bone formation. Here, we identified CXCL12 as a critical contributor to pathological new bone formation through recruitment of osteogenic precursor cells (OPCs). CXCL12 was found highly expressed in the regions that would potentially develop pathological new bone. OPCs were recruited to the regions where CXCL12 was up-regulated. Inhibition of CXCL12/CXCR4 axis with AMD3100 or conditional knockout of CXCR4 attenuated OPCs migration and subsequent pathological new bone formation in animal models of AS. By contrast, a genetically engineered animal model with CXCL12 overexpression developed a joint ankylosis phenotype. Furthermore, Rac1 was found essential for OPCs migration and pathological new bone formation. These findings ravel the novel role of CXCL12 in AS and indicate a potential strategy for targeting the CXCL12/CXCR4-Rac1 axis to prevent progression of axial skeleton ankylosis.

INTRODUCTION

Ankylosing spondylitis (AS) was first recognized in ancient Egypt as a phenotype of severe spinal kyphotic deformity at an advanced stage. Formerly known as Bechterew's disease, AS is currently defined as a subtype of axial spondyloarthritis (SpA) category with chronic progressive spinal inflammatory arthritis and ankylosis (also termed radiographic axial SpA) (*1*). The estimated prevalence of AS varies from 0.01 to 1.8% worldwide (*2*), and more patients with AS are male (the approximate male-to-female ratio is 2 to 3:1) (*2*–*4*). AS is characterized by inflammatory back pain, radiographic sacroiliitis, and excess spinal bone formation, leading to high morbidity and tremendous socioeconomic costs (*2*).

Inflammation and ankylosis are two manifestations of the disease. (*5*). Current therapies with nonsteroidal anti-inflammatory drugs and biologic agents, including tumor necrosis factor inhibitors (TNFi), interleukin-17 inhibitors (IL-17i), and, more recently, Janus kinase inhibitors, have led to substantial improvements in clinical symptoms and quality of life (*6*–*8*). Besides, recent studies show that TNFi or IL-17i have the potential to halt new bone formation when given early and in a sustained way (*6*, *7*). However, despite all recent advances in training of physicians and in imaging, a diagnostic delay remains a concern for patients with AS (*9*). For those patients in whom disease activity has been already too high for too long or in whom the process of bone remodeling already has started and solely stopping inflammation will not suffice anymore, no targeted treatment to retard the progression of disease at the level of bone structure is currently available (*10*). Late-stage patients with severe spinal kyphosis often required high-risk corrective surgery with various complication. Therefore, new therapies for this substantial unmet clinical need are urgently demanding.

The enthesis, which is the point where tendon, ligament, capsule, or fascia connect to bone, has been shown through accumulating evidence as the region of new pathological bone formation (*11*). The entheses transduce mechanical stress to the bone and appear to be prone to inflammation. Inflammation-activated cytokines instigate an inflammatory response and lead to bone apposition and the formation of enthesophytes through an uncertain mechanism (*12*). Elucidation of pathogenetic factors is important for identifying targets for intervention. Our and others' previous studies have found a variety of important factors in the entheseal microenvironment related to pathological new bone formation, including inflammation, growth factor signaling cascades, and abnormal mechanical transduction (*5*, *13*–*15*). In this bone-forming microenvironment, osteogenic precursor cells (OPCs) are considered responsive cells that commit ossification. Both resident and recruited OPCs are proposed to contribute to pathological new bone formation (*11*, *16*, *17*). Despite the source of osteogenic progenitors being a matter of considerable debate, how these cells migrate to the sites of new bone formation remains unclear. Understanding the underlying mechanism of OP migration may shed more light on the pathogenesis of new bone formation in AS and provide a potential therapeutic target for slowing ankylosis progression.

C-X-C motif chemokine ligand 12 (CXCL12) is a chemokine protein expressed in many tissues. Interacting with its receptor CXCR4, CXCL12-mediated cell migration has been demonstrated to participate in numerous physiological and pathological processes. It has been widely reported that in the skeleton, CXCL12 plays critical roles in bone homeostasis, cartilage development and regeneration, fracture repair, and onset of arthritis, including rheumatoid arthritis and osteoarthritis, through its homing effects on immune cells and OPCs (*18*–*21*). In addition, CXCL12 has been tentatively applied in

[1]Department of Spine Surgery, The First Affiliated Hospital, Sun Yat-sen University, Guangzhou, 510080 Guangdong, China. [2]Guangdong Province Key Laboratory of Orthopaedics and Traumatology, Guangzhou, 510080 Guangdong, China. [3]Department of Rheumatology and Immunology, The First Affiliated Hospital, Sun Yat-sen University, Guangzhou, 510080 Guangdong, China. [4]Department of Spine Surgery, The Fifth Affiliated Hospital, Sun Yat-sen University, Guangzhou, 510080 Guangdong, China.
*Corresponding author. Email: liuhui58@mail.sysu.edu.cn
†These authors contributed equally to this work.

tissue engineering for bone defects (*22*). However, whether CXCL12/CXCR4 signaling is involved in pathological new bone formation in AS remains unknown.

In this study, we identified CXCL12 as a critical contributor to pathological new bone formation in AS through recruitment of OPCs in a CXCL12/CXCR4-Rac1–dependent manner. Inhibition of CXCL12/CXCR4-Rac1 significantly suppresses OPCs migration and subsequent new bone formation both in vitro and in vivo, while a genetically engineered animal model with CXCL12 overexpression develops a joint ankylosing phenotype. These findings advance the understanding of the molecular mechanism of pathological new bone formation in AS and reveal the previously unidentified role of CXCL12 in this pathological process.

RESULTS

CXCL12 is up-regulated in entheseal and ligament tissues from patients with AS and animal models

Spinal ligament tissues from patients with AS and age- and sex-matched controls who underwent correction surgeries were collected (Fig. 1, A and B). Immunohistochemical staining showed that CXCL12 was aberrantly up-regulated in the AS group (Fig. 1, C and D). Serum level of CXCL12 was also up-regulated in patients with AS compared to nonradiographic SpA patients and non-AS patients (Fig. 1E). Three animal models for the studies of enthesitis with the phenotype of pathological new bone formation with different hypothetical pathogenesis of AS were successfully established: (i) proteoglycan-induced spondylitis (PGIS) mouse model in which autoantigens at spinal entheseal sites initiate self-sustaining immune reactions in susceptible strains that eventually lead to reactive new bone formation and spinal ankylosis (Fig. 1, F and G, and fig. S1, A to C); (ii) male DBA/1 spontaneous arthritis model which develops enthesitis and new bone formation due to their susceptible genetic background, spontaneous inflammation, aggressive behaviors, and sex-related hormones (Fig. 1, H and I, and fig. S1, D to F); and (iii) semi-Achilles tendon transection (SMTS) mouse model, which develop enthesopathy and new bone formation due to unbalanced mechanical loading (fig. S1, G to I). CXCL12 was up-regulated in these three animal models (Fig. 1, J to M, and fig. S2).

Although the DBA/1 model is a widely used model for the studies of enthesitis and entheseal ankylosis, different anatomic locations have been used to observe new bone formation (*23*–*25*), which may be inconsistent among different research groups. We further compared the incidence of pathological new bone formation in different anatomic locations and found that most pathological new bone developed on the plantar surfaces (fig. S2F) and dorsal surfaces (fig. S2H) of the hind paws.

CXCL12/CXCR4 induces migration of OPCs

To investigate whether CXCL12 functions as a mediator of OPC migration for new bone formation, colocalization of OPC markers [platelet-derived growth factor receptor α (PDGFRα) for human OPCs and stem cells antigen 1 (Sca1)/paired-related homeobox 1 (Prx1) for rodent OPCs] and CXCL12 was determined with immunohistochemical and immunofluorescence staining of tissues obtained from patients with AS and animal models. The results show that OPCs accumulated at the sites where CXCL12 was aberrantly expressed in human tissues (Fig. 2, A and B), PGIS model (Fig. 2, C to F, and fig. S3, A and B), DBA/1 model (Fig. 2, G to J, and fig. S3, C to F), and SMTS model (fig. S3, G to J). To further confirm that the recruitment of OPCs was mediated by CXCL12, a parabiosis mouse model was established by surgically joining green fluorescent protein (GFP) mice with 16-week-old DBA/1 mice. Parabionts were surgically joined (Fig. 2, K to L) and survived for 4 weeks to allow sharing circulation. After 1 month of feeding, both $CXCL12^+$ cell and GFP^+ cell enrichment occurred at the entheses in DBA/1 mice (Fig. 2, M to O, and fig. S5, I and J). These findings indicate that CXCL12/CXCR4 induces the migration of OPCs to the location of pathological new bone formation.

Inhibition of CXCL12/CXCR4 attenuates OPC migration and pathological new bone formation

To validate the critical role of CXCL12 in pathological new bone formation, we systemically administered the pharmacological inhibitory compound AMD3100 to all three animal models. The results show that pathological new bone formation was significantly suppressed by AMD3100 in the PGIS model, as determined by micro–computed tomography (μCT) analysis (Fig. 3, A and B). In addition, the number of recruited OPCs was reduced in the PGIS model, as determined by hematoxylin and eosin (H&E) staining and immunofluorescence staining (Fig. 3, C to F). Similar suppression was observed in the DBA/1 model (Fig. 3, G to L, and fig. S4, A to C) and SMTS model (fig. S4, D to H).

To confirm that the migration of OPCs mediated by the CXCL12/CXCR4 axis is critical for subsequent new bone formation, a $CXCR4^{fl/fl}$;*Prx1-creERT* mouse model was constructed ($CXCR4^{prx1}$), in which $Prx1^+$ OPCs no longer expressed CXCR4. These mice were backcrossed with DBA/1 mice for seven generations to retain the genetic background of DBA/1 mice and the nature of spontaneous arthritis onset. Compared to the control of seventh-generation backcrossed offspring of $CXCR4^{fl/fl}$ mice, both pathological new bone formation (Fig. 3, M and N) and the accumulation of OPCs were significantly reduced in $CXCR4^{prx1}$ mice (Fig. 3, O to R, and fig. S5, A to C). Similar findings were observed in the SMTS model established with $CXCR4^{prx1}$ mice (fig. S5, D to H).

The CXCL12-ERK1/2 (extracellular signal–regulated kinase 1/2) signaling cascade has been reported to be osteoinductive (*19*). To exclude the probability that the reduced new bone formation by inhibition of CXCL12/CXCR4 is dependent on the osteoinductive effect, the ERK1/2 inhibitor PD98059 was used in the animal models. The results showed that PD98059 had no significant suppressive effect on pathological new bone formation (fig. S6, A and B) and the accumulation of OPCs (fig. S6, C to E) in the PGIS model. A similar effect was observed in the DBA/1 model (fig. S6, F to J) and SMTS model (fig. S6, K to M). These results further confirmed that CXCL12-mediated migration of OPCs, other than its osteoinductive function, promoted pathological new bone formation.

The CXCL12/CXCR4 axis mediates OPC migration through Rac1

Downstream Rho–guanosine triphosphatase (GTPase) activation of CXCL12/CXCR4 is critical for the migration (*26*). To clarify the key members of the Rho family of GTPases that mediate CXCL12/CXCR4-induced OPC migration, specific inhibitors of cell division control protein 42 homolog (CDC42) (ML141), rac family small GTPase 1 (Rac1) (EHT1864), and Rho-associated, coiled-coil containing protein kinase (ROCK) (Y27632) were applied in a Transwell chamber assay. The results show that the migration of human bone marrow

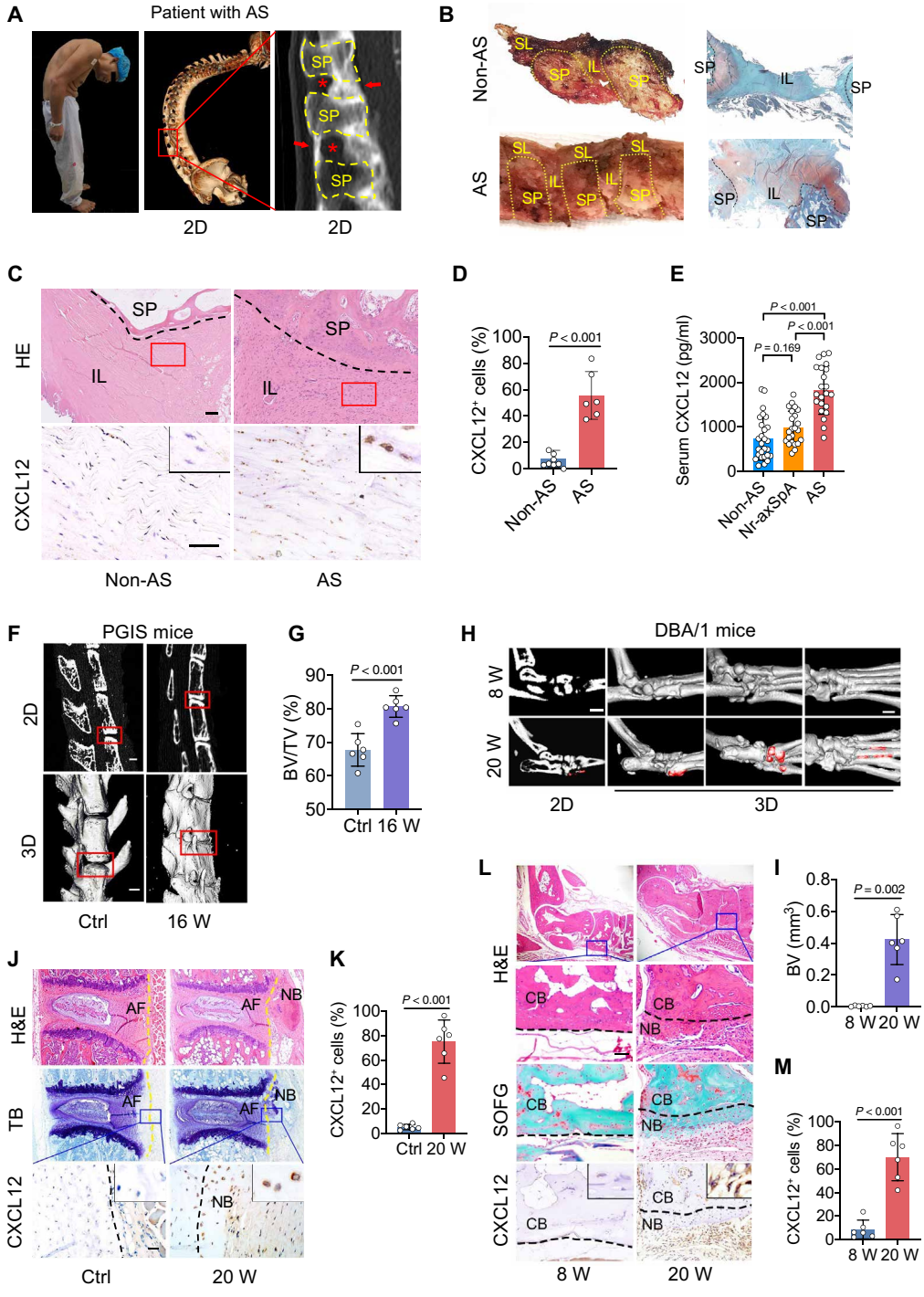

Fig. 1. CXCL12 is up-regulated in spinal ligament tissues from patients with AS and animal models. (**A**) Illustration of human spinal ligament tissue collection. Red arrows indicate pathological new bone. Red asterisks indicate uncalcified ligaments, the potential pathological new bone formation sites, that are used for further analysis. 2D, two dimensional. (**B**) Schematic diagram of the anatomy of the spinal ligament. (**C** and **D**) Hematoxylin and eosin (H&E) staining, immunohistochemical staining, and quantitative analysis of CXCL12 in spinal ligament from patients with AS and non-AS patients. Scale bars, 200 μm. (**E**) Peripheral serum concentration of CXCL12 of non-AS ($n = 27$), non-radiographic axial spondyloarthritis (Nr-axSpA) ($n = 23$), and patients with AS ($n = 22$). Analysis of variance (ANOVA; $F_{2,69} = 34.69$) with Tukey's post hoc test was used. (**F** and **G**) Micro–computed tomography (μCT) images and quantitative analysis of lumber spine of PGIS mice. Scale bars, 500 μm. (**H** and **I**) μCT images and quantitative analysis of hind paw of DBA/1 mice at the age of 8 and 20 weeks (W). Scale bars, 1 mm. (**J** and **K**) H&E staining, TB staining, immunohistochemical staining, and quantitative analysis of CXCL12 in lumber spine of PGIS mice. Scale bar, 200 μm. (**L** and **M**) H&E staining, Safranin O and Fast Green (SOFG) staining, immunohistochemical staining, and quantitative analysis of CXCL12 in hind paws of male DBA/1 model. Scale bar, 200 μm. Each dot represents the mean value of three technical replicates. $n = 6$ tissues from six patients with AS versus $n = 8$ tissues from eight non-AS patients in (A to D). $n = 6$ tissues from six mice for each group in (C to L). Data are shown as means ± SEM. Student's t test with Shapiro-Wilk test was used unless specifically mentioned. CB, cortical bone; NB, new bone; SP, spinous process; IL, interspinous ligament; SL, supraspinous ligament; BV, bone volume; TV, total volume; TB, toluidine blue.

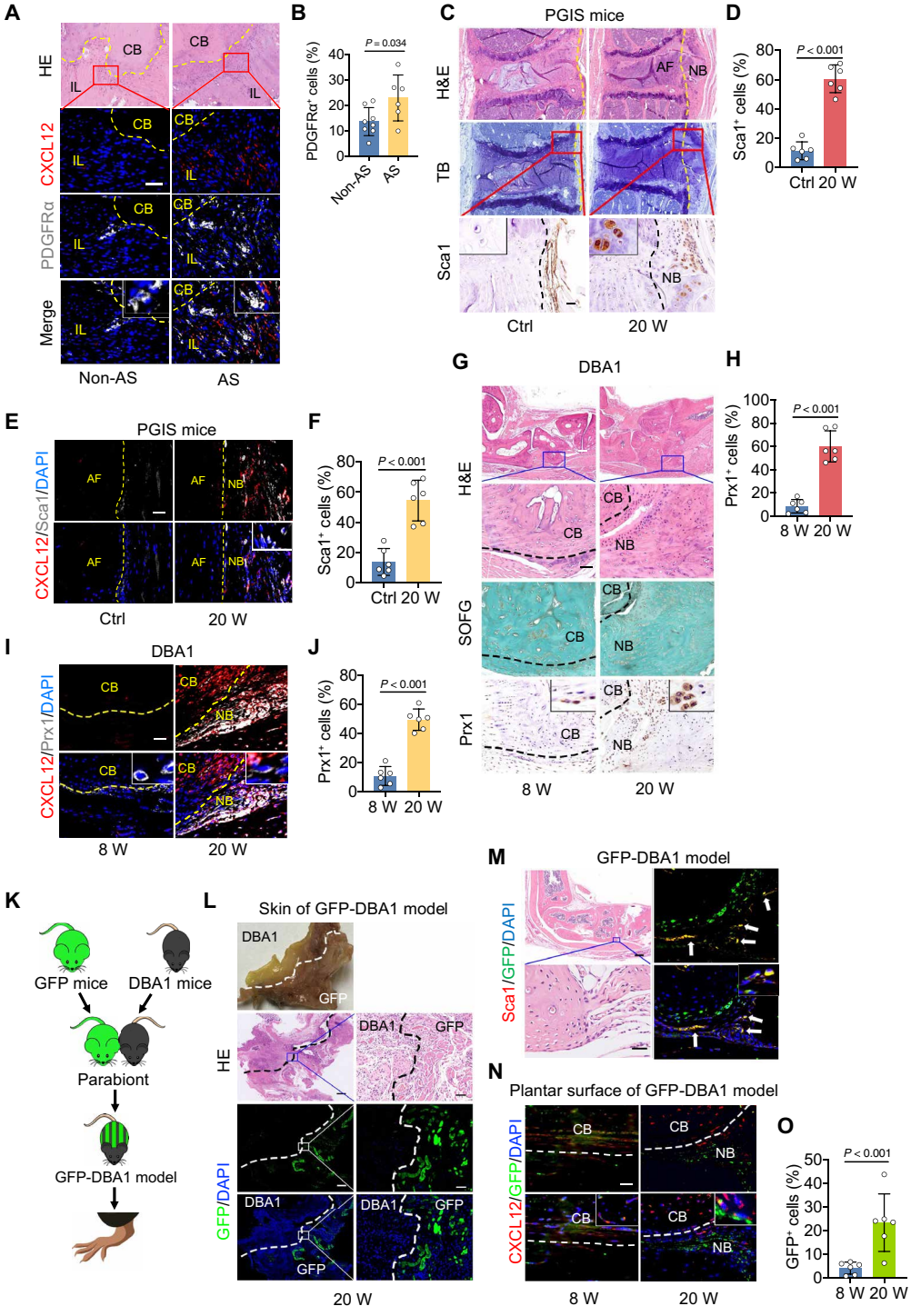

Fig. 2. CXCL12/CXCR4 induces migration of OPCs. (**A** and **B**) Immunofluorescence staining and quantitative analysis of PDGFRα in spinal tissues from patients with AS or non-AS. Scale bar, 100 μm. $n = 6$ tissues from patients with AS versus $n = 8$ tissues from non-AS patients. (**C** and **D**) H&E staining, TB staining, immunohistochemical staining, and quantitative analysis of Sca1 in spine of PGIS mice. Scale bar, 100 μm. $n = 6$ per group. (**E** and **F**) Immunofluorescence staining and quantitative analysis of Sca1 in spine of PGIS mice. Scale bar, 20 μm. $n = 6$ per group. (**G** and **H**) H&E staining, SOFG staining, immunohistochemical staining, and quantitative analysis of Prx1 in hind paws of male DBA/1 model at the age of 8 and 20 weeks. Scale bar, 200 μm. $n = 6$ per group. (**I** and **J**) Immunofluorescence staining and quantitative analysis of Prx1 in hind paws of male DBA/1 model. Scale bar, 20 μm. $n = 6$ per group. (**K**) Schematic diagram of the construction process of GFP-DBA/1 mice parabiosis. (**L**) H&E staining and immunofluorescence analysis of GFP in the skin tissues of GFP-DBA/1 mice. Scale bars, 500 μm. (**M**) H&E staining, immunofluorescence analysis of GFP and Sca1 in GFP-DBA/1 mice. Scale bars, 50 μm. $n = 6$ per group. (**N** and **O**) Immunofluorescence staining and quantitative analysis of GFP and CXCL12 in the plantar surface of hind paws of GFP-DBA/1 model at the age of 8 and 20 weeks. $n = 6$ per group. Scale bar, 100 μm. Data are shown as means ± SEM. Student's *t* test with Shapiro-Wilk test was used. DAPI, 4′,6-diamidino-2-phenylindole.

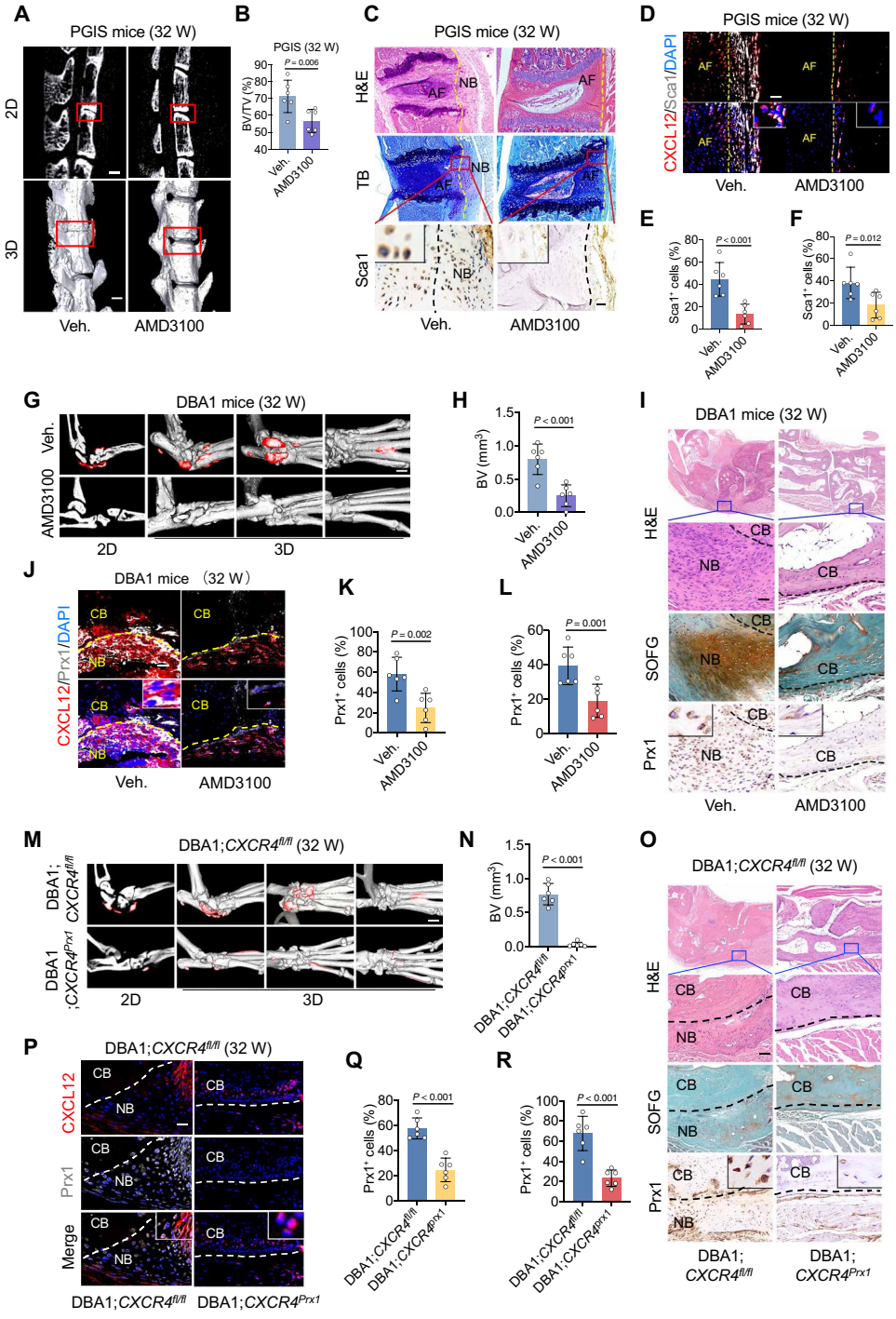

Fig. 3. Inhibition of CXCL12/CXCR4 attenuates OPC migration and pathological new bone formation. (**A** and **B**) μCT images and quantitative analysis of pathological new bone formation in spine of PGIS mice. Scale bars, 500 μm. $n = 6$ per group. Veh., vehicle. (**C**) H&E staining, TB staining, immunohistochemical staining of Sca1 in spine of PGIS mice at the age of 32 weeks after AMD3100 administration. Scale bar, 200 μm. $n = 6$ per group. (**D**) Immunofluorescence staining of Sca1 and CXCL12 in PGIS mice. Scale bar, 20 μm. $n = 6$ per group. (**E**) Quantitative analysis of Sca1 in (C). (**F**) Quantitative analysis of Sca1 in (D). (**G** and **H**) μCT images and quantitative analysis of pathological new bone formation in hind paw of male DBA/1 model at the age of 32 weeks after AMD3100 administration. Scale bar, 500 μm. $n = 6$ per group. (**I**) H&E staining, SOFG staining, and immunohistochemical staining of Prx1 in hind paw of male DBA/1 model. Scale bar, 200 μm. $n = 6$ per group. (**J**) Immunofluorescence staining of Prx1 and CXCL12 in hind paw of male DBA/1 mice. Scale bar, 20 μm. $n = 6$ per group. (**K**) Quantitative analysis of Prx1 in (J). (**L**) Quantitative analysis of Prx1 in (I). (**M** and **N**) μCT images and quantitative analysis of pathological new bone formation in hind paw of DBA/1;CXCR4$^{fl/fl}$ mice and DBA/1;CXCR4^{prx1} mice. Scale bar, 500 μm. (**O**) H&E staining, SOFG staining, immunohistochemical staining of Prx1 in DBA/1;CXCR4$^{fl/fl}$ mice and DBA/1;CXCR4^{prx1} mice. Scale bar, 100 μm. $n = 6$ per group. (**P**) Immunofluorescence staining of Prx1 and CXCL12 in hind paw of DBA/1;CXCR4$^{fl/fl}$ mice and DBA/1;CXCR4^{prx1} mice. Scale bar, 20 μm. $n = 6$ per group. (**Q**) Quantitative analysis of Prx1 in (P). (**R**) Quantitative analysis of Prx1 in. (O) Data are shown as means ± SEM. Student's *t* test with Shapiro-Wilk test was used. AMD3100, CXCR4 inhibitor.

mesenchymal stem cells (hBMSCs) induced by CXCL12 (100 ng/ml) was significantly inhibited by AMD3100 and EHT1864, while ML141 and Y27632 had no significant inhibitory effect on cell migration (fig. S7, A to C). In vivo, the Rac1 inhibitor EHT1864 was administered systemically to all three animal models. The results indicate that pathological new bone formation and OPC recruitment were significantly reduced in the PGIS model, as determined by μCT analysis (Fig. 4, A and B), H&E staining, and immunohistochemical

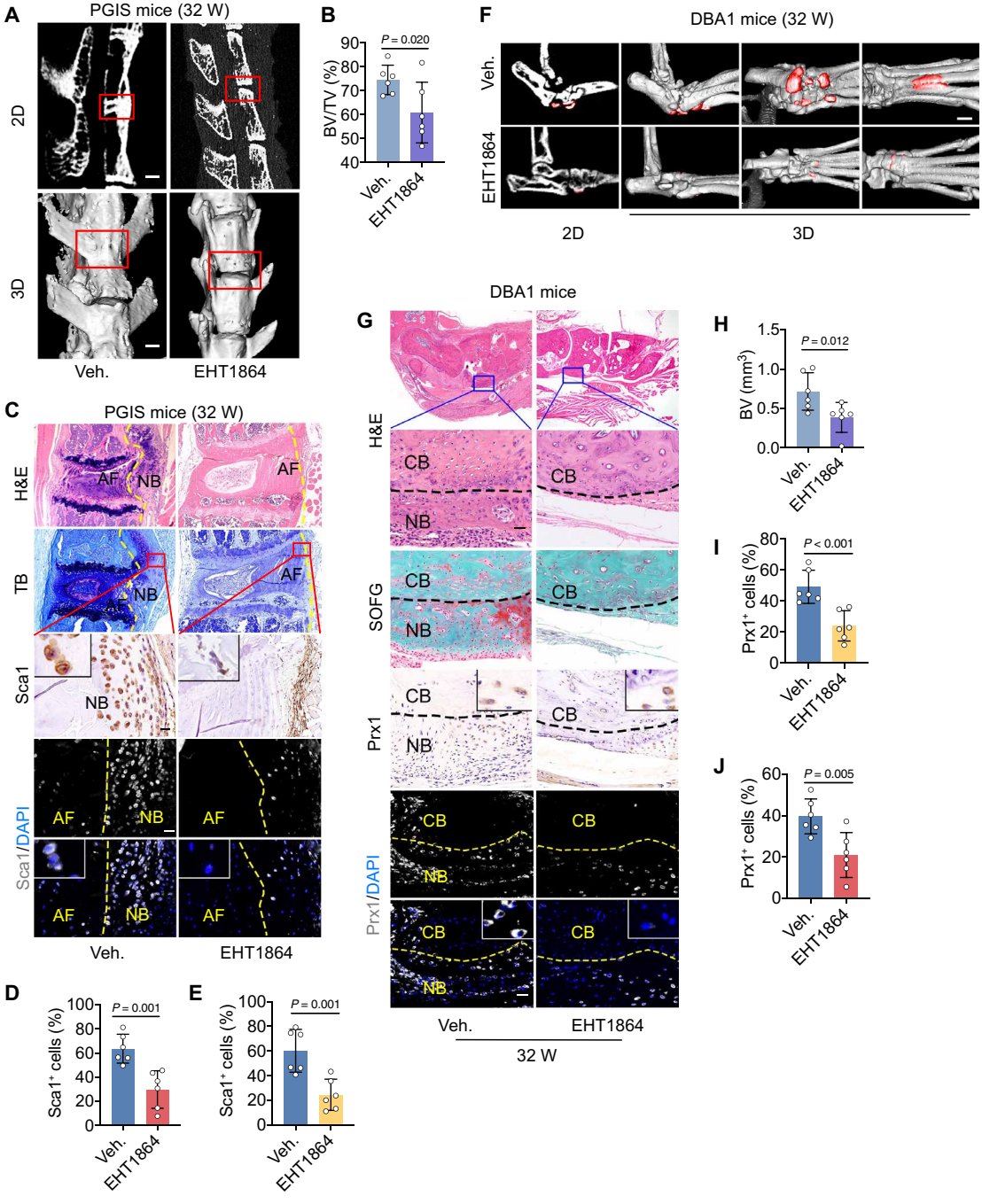

Fig. 4. The CXCL12/CXCR4 axis mediates OPC migration through Rac1. (**A** and **B**) μCT images and quantitative analysis of pathological new bone formation in PGIS mice at the age of 32 weeks after EHT1864 administration. Scale bars, 500 μm. $n = 6$ per group. (**C**) H&E staining, TB staining, immunohistochemical staining, and immunofluorescence staining of Sca1 in PGIS mice. Scale bars, 100 μm. $n = 6$ per group. (**D** and **E**) Quantitative analysis of Sca1 in (C). (**F**) μCT images of pathological new bone formation in hind paw of male DBA/1 mice at the age of 32 weeks after EHT1864 administration. Scale bar, 50 μm. $n = 6$ per group. (**G**) H&E staining, SOFG staining, immunohistochemical staining, and immunofluorescence staining of Prx1 in plantar surface of hind paw of male DBA/1 mice at the age of 32 weeks after EHT1864 administration. Scale bars, 50 μm. $n = 6$ per group. (**H**) Quantitative analysis of pathological new bone formation in (F). (**I** and **J**) Quantitative analysis of Prx1 in (G). Data are shown as means ± SEM. Student's *t* test with Shapiro-Wilk test was used. EHT1864, Rac1 inhibitor.

staining (Fig. 4, C to E). Similar reduction was observed in the DBA/1 model (Fig. 4, F to J, and fig. S8, A to C) and SMTS model (fig. S8, D to I). The above results suggested that Rac1 is the critical mediator of CXCL12/CXCR4 axis–induced OPCs migration and pathological new bone formation.

CXCL12 is majorly produced by CD45$^+$ immune cells in the inflammatory phase and Col2a1$^+$ cells in the endochondral ossification phase

To illustrate the source of CXCL12, dynamic changes in immune cells and mesenchymal cells at the sites of new bone formation were detected by immunofluorescence staining with multiple cell surface markers in PGIS mice and DBA/1 mouse models. The results showed that in the early stages as inflammatory phase, CXCL12$^+$ cells were primarily costained with CD45$^+$ immune cells in the PGIS model. Subsequently, the number of CXCL12$^+$ CD45$^+$ cells declined with the resolution of inflammation (Fig. 5, A and B). In the late stage as bone formation phase, CXCL12$^+$ cells were primarily costained with Col2a1$^+$ cells (Fig. 5, C and D), which were abundant in the process of endochondral ossification. Similar results were observed in the DBA/1 model (fig. S9, A to D). In the uncalcified spinal ligament tissues (supraspinous ligament and interspinous ligament) from patients with AS, immunofluorescence staining results showed that CXCL12$^+$ cells were primarily costained with CD45$^+$ immune cells and Col2a1$^+$ cells (Fig. 5, E to H). To investigate the cells expressing CXCL12 among CD45$^+$ cells, single-cell sequencing analysis of spinal ligament tissues collected from patients with AS who underwent corrective surgeries were performed. After application of quality control filters, single cells were obtained and single-cell sequencing was performed. Gene expression data were aligned to be projected in a two-dimensional space through *t*-stochastic neighbor embedding, and seven clusters were identified, including macrophage, lymphocyte, mesenchymal stromal cell (MSC), tenocyte, osteoblast, chondrocyte, endothelial cell, and muscle cell (fig. S10A). Among CD45$^+$ immune cells, CXCL12 was found mainly expressed in CD68$^+$ macrophages (fig. S10B). In addition, immunofluorescence analysis further confirmed that CXCL12 was mainly expressed in CD68$^+$ macrophages in the spinal ligament tissues from patients with AS (fig. S10, C and D). Similarly, CXCL12 was found mainly expressed in F4/80$^+$ macrophages in animal models (fig. S10, E and F).

Previous studies suggest that among the AS-associated cytokines (TNFα, IL-17A, IL-22, and IL-23), IL-17 can induce CXCL12 expression in follicular stromal cells, while and TNFα stimulate expression of CXCL12 in astrocytes (*27*). TNFα, IL-17A, and IL-22 signaling have been implicated in AS pathology (*12*, *28*, *29*). To investigate whether these inflammatory cytokines could modulate the expression of CXCL12 in macrophages, we obtained F4/80$^+$ macrophages from C57BL6/J mice through digestion of the spleen and flow cytometry sorting. The cells were cultured and stimulated with different AS-associated cytokines (TNFα, IL-17A, IL-22, and IL-23); then, expression of CXCL12 was determined by reverse transcription quantitative polymerase chain reaction (RT-qPCR) analysis. The results showed that TNFα and IL-17A increased while IL-22 and IL-23 did not significantly affect the expression of CXCL12 (fig. S10G). In addition, to investigate cytokine expression modification after CXCL12 inhibition, the cells were stimulated with CXCL12 with or without CXCR4 antagonist AMD3100, and the expression of the above cytokines was determined by RT-qPCR analysis. The results showed that CXCL12 promoted expression of TNFα and IL-17A, while administration of AMD3100 suppressed this inductive effect (fig. S10, H to K). These results suggest that TNFα and IL-17A could induce CXCL12 overexpression in a feedforward manner.

DBA/1;CXCL12^{col2} mice develop an ankylosis phenotype

To confirm the critical role of CXCL12 in pathological new bone formation, we constructed a *CXCL12$^{hi/hi}$;Col2a1-creERT* mouse model (*CXCL12^{col2}*), in which Col2a1$^+$ cells expressed highly CXCL12. These mice were backcrossed with DBA/1 mice for seven generations to maintain the genetic background and features of spontaneous arthritis. *DBA/1;CXCL12^{col2}* mice showed a more severe phenotype of entheseal new bone formation (Fig. 6, A and B) and enhanced recruitment of OPCs (Fig. 6, C to E, and fig. S11, A to C) than seventh-generation backcrossed offspring of *CXCL12$^{fl/fl}$* mice at the same observation time points. A similar phenotype was observed in the SMTS model constructed with *CXCL12^{col2}* mice (fig. S11, D to G). Because of the lower incidence of spinal ankylosis in the PGIS model, genetic backcross is nearly impossible to generate a PGIS model in knock-in mice. However, upon tamoxifen induction, the *CXCL12^{col2}* mice developed spontaneous arthritis and spondylitis, followed by ankylosis and spinal kyphosis due to pathological new bone formation, which was similar to the clinical features of AS (Fig. 6, F to K). To confirm that the CXCL12/CXCR4-Rac1 axis was critical in this knock-in model, the Rac1 inhibitor EHT1864 was systemically administered to different models. The results show that the pathological new bone formation (Fig. 6, A and B) and the enhanced recruitment of OPCs (Fig. 6, C to E, and fig. S11, A to C) were significantly attenuated with EHT1864 treatment in the DBA/1 model. A similar phenotype was observed in the SMTS model (fig. S11, D to G) and PGIS model (Fig. 6, F to K).

DISCUSSION

Immobilization of the axial skeleton due to pathological new bone formation is a critical manifestation of AS, leading to disability and with no satisfactory solution to date. Although accumulating studies have revealed important environmental factors that favor new bone formation, how OPCs migrate to the regions that finally ossify is still unknown.

CXCL12-mediated OPCs migration has been reported to contribute to cartilage and bone formation in different situations (*18*, *20*, *22*). Since CXCL12 is up-regulated in various inflammatory conditions and AS is a chronic inflammatory disease, it is reasonable to speculate that CXCL12 may contribute to the pathological process of new bone formation in AS (*21*). In the current study, we observed that CXCL12 was highly expressed in the ligament and entheseal tissues from patients with AS and animal models, which were the regions that would potentially develop pathological new bone. OPCs were recruited to the region where CXCL12 was up-regulated in these tissues. Inhibition of the CXCL12/CXCR4 axis with the pharmacological inhibitor AMD3100 or conditional knockout of CXCR4 in OPCs significantly attenuated OP migration and subsequent pathological new bone formation. These findings strongly suggest that CXCL12/CXCR4-mediated OPC migration plays a critical role in pathological new bone formation in AS.

The responsive cells for pathological new bone are thus far unclear. Previous studies suggest that both resident and remote progenitor cells may contribute to the development of pathological new bone (*11*, *17*). Histological studies showed that most entheses

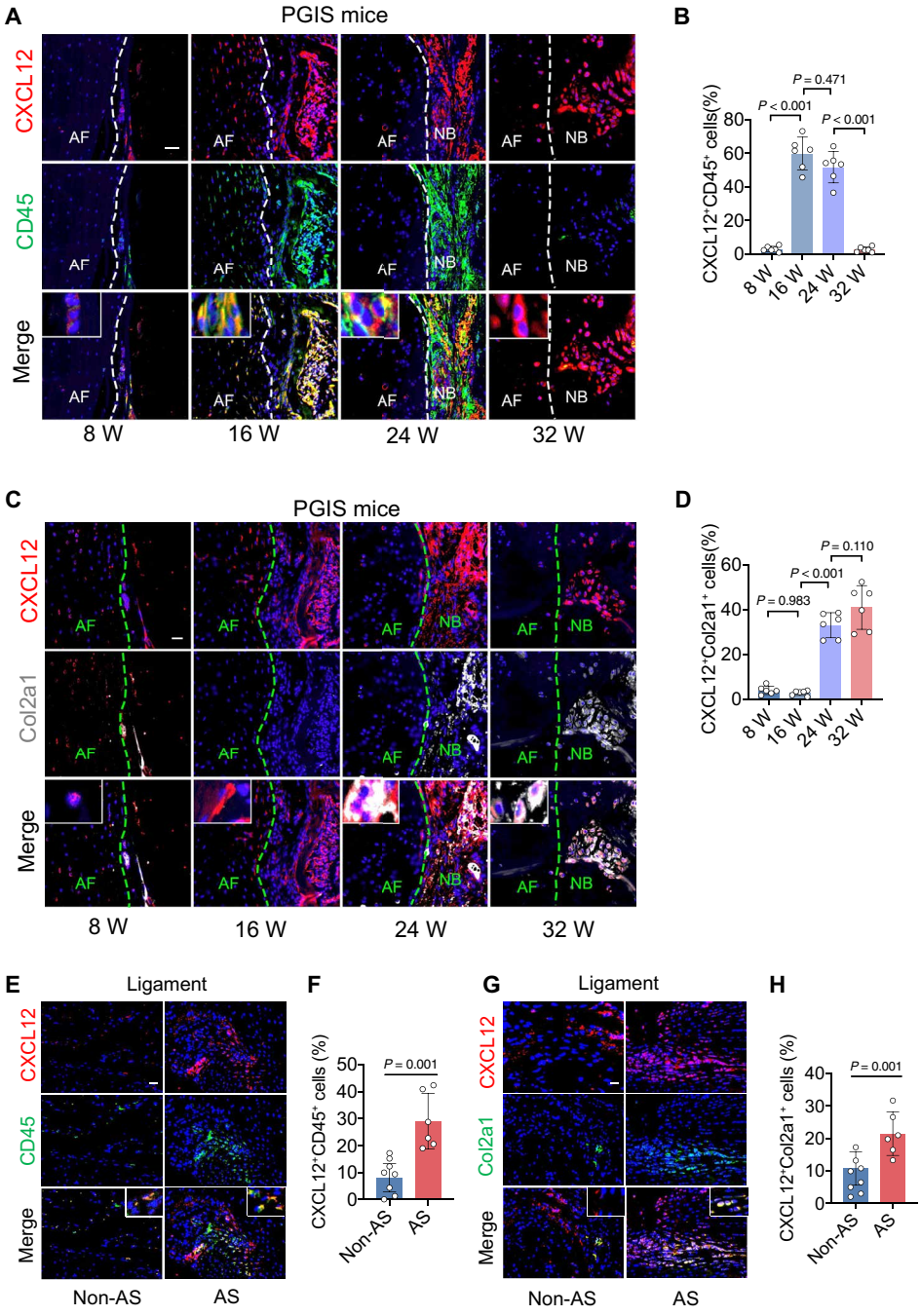

Fig. 5. CXCL12 is majorly produced by CD45$^+$ cells in the inflammatory phase and Col2a1$^+$ cells in the endochondral ossification phase. (**A** and **B**) Immunohistochemical staining and quantitative analysis of CXCL12 and CD45 in PGIS mice at the age of 8, 16, 24, and 32 weeks. Scale bar, 20 μm. $n = 6$ per group. ANOVA ($F_{3,20} = 121.10$) with Tukey's post hoc test was used. (**C** and **D**) Immunohistochemical staining and quantitative analysis of CXCL12 and Col2a1 in PGIS mice at the age of 8, 16, 24, and 32 weeks. Scale bar, 20 μm. $n = 6$ per group. ANOVA ($F_{3,20} = 71.24$) with Tukey's post hoc test was used. (**E** and **F**) Immunohistochemical staining and quantitative analysis of CXCL12 and CD45 in spinal ligament tissues of patients with AS and non-AS patients. Scale bar, 20 μm. $n = 6$ tissues from patients with AS versus $n = 8$ tissues from non-AS patients. Student's t test with Shapiro-Wilk test was used. (**G** and **H**) Immunohistochemical staining and quantitative analysis of CXCL12 and Col2a1 in spinal ligament tissues of patients AS and non-AS patients. Scale bar, 20 μm. $n = 6$ tissues from patients with AS versus $n = 8$ tissues from non-AS patients. Student's t test with Shapiro-Wilk test was used. Data are shown as means ± SEM.

have small holes in the destructive cortical shell, allowing migration of OPCs from the adjacent bone marrow to entheses (*30*). However, whether remote or circulating OPCs are involved in the process of pathological new bone formation is unknown. In this study, results from a parabiosis mouse model confirmed that remote osteoprogenitor cells entered circulation and contribute to pathogenic new bone formation. Because of the lack of generally accepted markers to identify resident or remote osteoprogenitors, it is unlikely for the

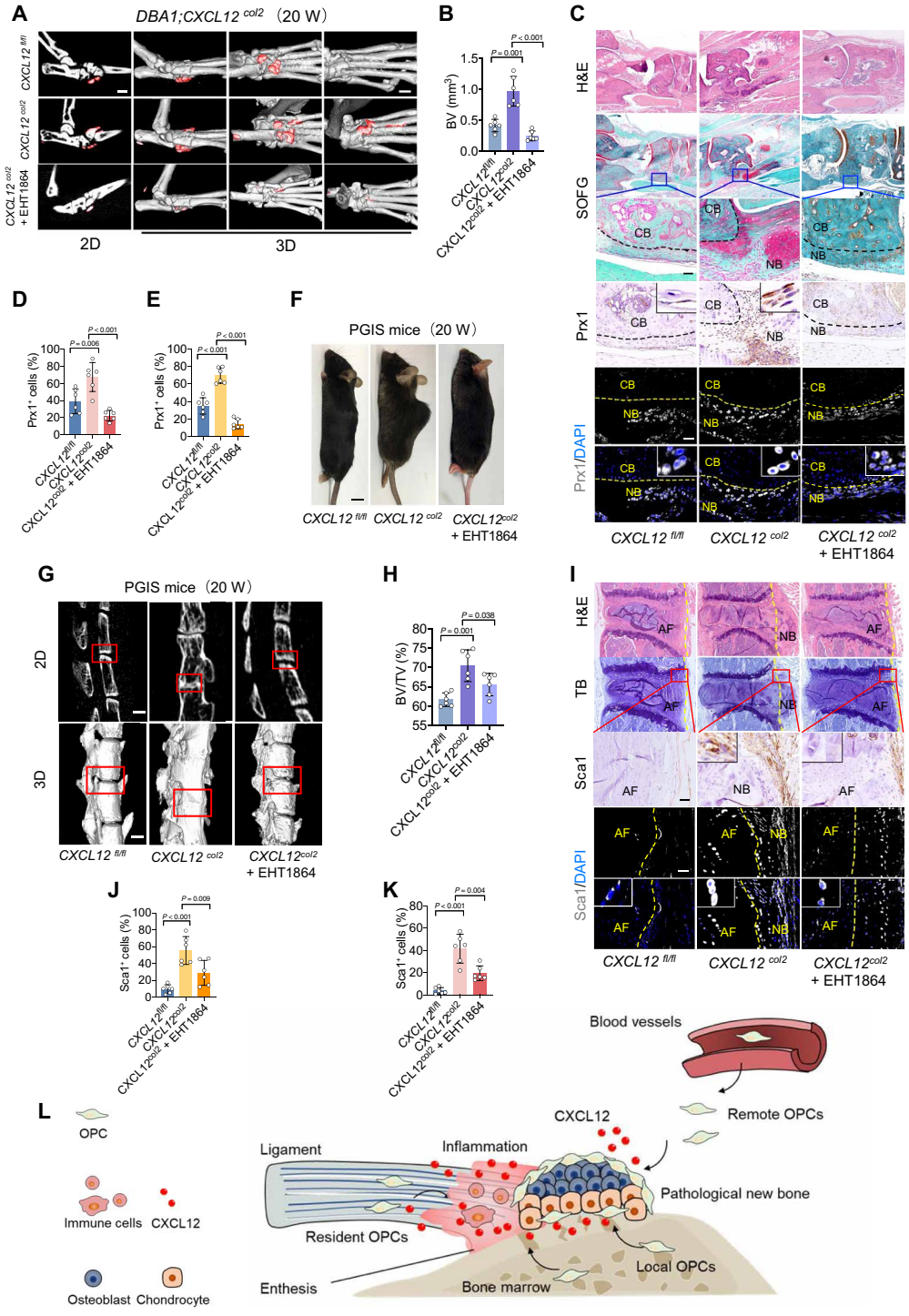

Fig. 6. CXCL12$^{Col2\text{-}cre}$ mice develop an ankylosis phenotype. (**A** and **B**) μCT images and quantitative analysis of pathological new bone formation in hind paw of DBA/1;CXCL12^{Col2} mice at the age of 20 weeks with or without EHT1864 administration. Scale bars, 500 μm. $n = 6$ per group. ANOVA ($F_{2,15} = 34.40$). (**C**) H&E staining, SOFG staining, immunohistochemical staining, and immunofluorescence staining of Prx1 in plantar surface of hind paw of DBA/1;CXCL12^{Col2} mice at the age of 20 weeks with or without EHT1864 administration. Scale bars, 200 μm. $n = 6$ per group. (**D** and **E**) Quantitative analysis of Prx1 in (C). ANOVA ($F_{2,15} = 17.62$; $F_{2,15} = 71.39$). (**F**) Photo of CXCL12^{Col2} mice at the age of 20 weeks with or without EHT1864 administration. Scale bar, 5 mm. (**G** and **H**) μCT images and quantitative analysis of pathological new bone formation in the spine of CXCL12^{Col2} PGIS mice at the age of 20 weeks with or without EHT1864 administration. Scale bars, 200 μm. $n = 6$ per group. ANOVA ($F_{2,15} = 34.74$). (**I**) H&E staining, TB staining, immunohistochemical staining, and immunofluorescence staining of Sca1 in spine of CXCL12^{Col2} PGIS mice at the age of 20 weeks with or without EHT1864 administration. Scale bars, 200 μm. $n = 6$ per group. (**J** and **K**) Quantitative analysis of Sca1 in (I). ANOVA ($F_{2,15} = 29.55$; $F_{2,15} = 18.36$). (**L**) Schematic diagram illustrating CXCL12-induced pathological new bone formation and recruitment of OPCs. Data are shown as means ± SEM. One-way ANOVA with Levene's test, followed by the Tukey's post hoc test was used.

application of cell tracing techniques or cell-specific interventions to determine which osteoprogenitors most contribute to pathological new bone formation. Further investigations are needed to answer this question.

Members of the Rho family of GTPases are involved in the context of pseudopodium formation and cell migration, most notably Rho, Rac, and Cdc42 proteins (*31*). A previous study suggested that RhoA and Rac1 played key roles in CXCL12-induced adhesion and motility (*26*). In the current study, we found that Rac1 was the downstream regulator of CXCL12/CXCR4-mediated OPCs migration. Inhibition of Rac1 significantly attenuated OPC recruitment and pathological new bone formation in animal models of AS.

Multiple cell types have been shown to produce CXCL12 under inflammatory stimulation, including chondrocytes, macrophages, endothelial cells, and stromal cells (*32*). In this study, we found that CXCL12 was initially expressed by $CD45^+$ immune cells at the early phase, in which multiple immune cells infiltrated into the enthesis, leading to an inflammatory response. At the later stage, in which the immune cell number declined and pathological new bone developed in an endochondral ossification manner, CXCL12 was mainly expressed by $Col2a1^+$ cells. We therefore generated *CXCL12*$^{fl/fl}$*;Col2a1-creERT* mice. By backcrossing these mice with DBA/1 mice for seven generations, we established a model with spontaneous enthesitis and ankylosis phenotypes that overexpressed CXCL12 in $Col2a1^+$ cells. We found that these mice presented a more severe ankylosis phenotype with higher volume and earlier onset time of pathological new bone. As expected, more OPCs were recruited to the sites of new bone formation. Similar findings were observed in the SMTS model. Because of the lower morbidity of the PGIS model, we failed to establish a PGIS model with CXCL12 overexpression by backcrossing. However, we unexpectedly found that the CXCL12 conditional knock-in mice developed a phenotype with spinal kyphosis and ankylosis with pathological new bone formation in their elderly age without PG induction. Since CXCL12 is known to recruit immune cells, we speculate that long-lasting expression of CXCL12 would amplify and maintain the inflammatory response triggered by microdamage, which is the common pathological change of the enthesis under repeated mechanical strains. Persisting inflammation and entheseal microdamage trigger the tissue remodeling process and lastly lead to pathological new bone formation (*33*).

Chemokines are well known to regulate the migration and positioning of immune cells. CXCL12 has been shown to recruit immune cells, including myeloid cells and lymphocytes (*32*). Since accumulating evidence shows that inflammation and new bone formation are correlated, whether the suppressive effect of CXCL12 inhibition on new bone formation occurs through inhibition of inflammation needs to be further studied (*34*–*36*). In the current study, we found that the clinical severity score decreased with CXCL12 antagonist in DBA/1 mice, indicating that the CXCL12/CXCR4 axis also played a role in maintaining the inflammatory microenvironment. However, conditional knockout of CXCR4 in OPCs and EHT1864 administration resulted in less recruitment of OPCs and pathological new bone without influencing clinical severity score, confirming that CXCL12/CXCR4-mediated OPC recruitment is critical for pathological new bone formation.

The CXCL12-ERK1/2 signaling pathway has been reported to be osteoinductive (*19*). To further distinguish whether the osteoinductive or chemotactic effect of CXCL12 is the major mechanism responsible for pathological new bone formation, a CXCL12-ERK1/2 signaling antagonist was applied to determine its effect on chondrogenesis/osteogenesis and OPCs migration in animal models. The results showed that inhibiting ERK1/2 signaling could not suppress pathological new bone formation, suggesting that the chemotactic effect of CXCL12 was responsible for pathological new bone formation.

As no animal model completely mimics human disease, different questions can be raised regarding the relevance of the models to human SpA. At present, three categories of animal models of SpA are used: human leukocyte antigen (HLA)–B27/human β(2)-microglobulin transgenic rats (*37*); genetically engineered mouse models with high levels of inflammation, including human TNF transgenic mice, transmembrane TNF transgenic mice, and $TNF^{\Delta ARE}$ mice (*38*, *39*); and nongenetically engineered models. Among these models, nongenetic engineered models are widely used for the study of pathological new bone formation. In the current study, to better simulate the diversity of AS phenotypes, three different types of animal models of AS with different pathogeneses were established: (i) A PGIS mouse model that exhibits both axial and peripheral inflammation was established to observe pathological changes in the spine (*40*–*42*). Spinal ankylosis in the PGIS model is an autoimmune-induced pathological process and a unique model that exhibits an ankylosis phenotype in the spine except in genetically engineered mice (*41*). (ii) An aging DBA/1 arthritis animal model shares multiple similarities with AS in humans, including spontaneously developed enthesitis and entheseal new bone formation, because of its susceptible genetic background, spontaneous inflammation, aggressive behavior, and sex-related hormones (*23*, *25*). (iii) An SMTS model was established to study pathological new bone formation due to the disruption of mechanical stress transmission at the posterior calcaneal tuberosity, as mechanical stress plays a prominent role in experimental AS (*43*). All these animal models share the characteristics of ankylosing enthesitis, which is a feature of AS in humans. In all three models, CXCL12/CXCR4-Rac1–mediated OPCs migration was found to be critical for pathological new bone formation, suggesting that it is a common mechanism despite the heterogeneity of pathogenesis in AS.

Given that CXCL12/CXCR4 has been proven to be the major mechanism of various diseases, inhibiting CXCL12/CXCR4 with pharmaceutical compounds, such as plerixafor, BL-8040, and ulocuplumab, has been used as a therapy in several clinical trials for cancers, pancreatic diseases, and rheumatoid arthritis. Most of these trials reported mild to moderate adverse events, including gastrointestinal disorders, musculoskeletal and connective tissue disorders, nervous system disorders, and injection site reactions (*44*–*46*). Thus, given the full consideration of side effects and the means to address them, the application of CXCL12/CXCR4 inhibitors in AS is worth considering.

There are certain limitations in this study. First, although CXCL12 is up-regulated in patients with AS, to strengthen the possibility of using CXCL12 as a possible therapeutic target in AS, further clinical investigation with a large cohort is needed to clarify its correlation with disease activity, C-reactive protein (CRP) level, gender, HLA-B27 status, and radiographic characters. Second, for ethical reasons, all the tissue samples in this study were collected from patients with AS who developed severe spine ankylosis. Therefore, the conclusion regarding human tissues might not represent all patients with AS having different disease activities. In summary,

the novel findings of the current study suggest that CXCL12/CXCR4-Rac1–mediated migration of OPCs contributes to pathological new bone formation in AS.

MATERIALS AND METHODS

Human tissue

The institutional of ethics committee (IEC) for Clinical Research and Animal Trials of the First Affiliated Hospital of Sun Yat-sen University approved the procedures performed in this study (IDs: [2020]404 and [2021]740). Six patients with AS and eight non-AS volunteers were consecutively enrolled at the First Affiliated Hospital, Sun Yat-sen University between September 2017 and June 2021. Written informed consent was obtained from all subjects. The samples (bone, ligamentum flavum, supraspinatus ligament, and interspinous ligament) involved in spinal ankylosis from patients with AS and non-AS patients were obtained during spinal surgery, which was performed by senior surgeons.

Genetically modified mice

DBA/1 and C57BL/6J mice were purchased from the Charles River Laboratories. *CXCR4*$^{fl/fl}$ (C57BL/6J) conditional knockout mice were engineered via CRISPR-Cas system by GemPharmatech. The mouse *ROSA26* gene [National Center for Biotechnology Information (NCBI) reference sequence: NR_027008.1] and the mouse *CXCR4* gene (NCBI reference sequence: NC_000067.6) is located on mouse chromosome 1. The exon2 of the CXCR4-201 (ENSMUST00000052172.6) transcript was selected as the knockout region. *CXCL12*$^{fl/fl}$ (C57BL/6J) mice were created by Cyagen Biosciences via using CRISPR-Cas–mediated genome engineering. *CXCL12* gene (NCBI reference sequence: NM_001012477.2) is located on mouse chromosome 6. Transgenic mice expressing Cre recombinase under control of the paired related homeobox 1 promoter (*Prx1-CreERT*) knock-in mice were engineered via CRISPR-Cas system by GemPharmatech. The collagen type II alpha 1 promoter (*Col2a1-CreERT*) mice were engineered via CRISPR-Cas system by Cyagen Biosciences. *Prx1-CreERT* and *Col2a1-CreERT* mice were mated with *CXCR4*-floxed mice and *CXCL12*-floxed mice to obtain various *CXCR4*$^{fl/fl}$;*Prx1-creERT* (C57BL/6J) and *CXCL12*$^{fl/fl}$;*Col2a1-creERT* mice. *CXCL12*$^{fl/fl}$;*Col2a1-creERT* mouse model mice were backcrossed with DBA/1 mice for seven generations to retain the genetic background of DBA/1 mice. For postnatal activation of CreERT, tamoxifen (100 mg/kg; Sigma-Aldrich) in corn oil (Sigma-Aldrich) was intraperitoneally injected into mice once a day for seven consecutive days.

Mice models

PGIS mice were induced using previously described standard methods (*14*). Briefly, the first antigen injection (100 mg of PG protein) was given in complete Freund's adjuvant (Sigma-Aldrich, MO, USA), and the same doses of antigen were injected as second and third boosts in incomplete Freund's adjuvant on weeks 3 and 6.

DBA/1 mice and BALB/c mice were purchased from Charles River Laboratories. Nine of male DBA/1 mice were caged in one cage. Mice were euthanized at the same period time as the PGIS mice.

The SMTS mice model were constructed in wild-type (C57BL/6J), *CXCR4*$^{fl/fl}$;*Prx1-creERT* (C57BL/6J), and *CXCL12*$^{hi/hi}$;*Col2a1-creERT* (C57BL/6J) mice. The procedure of SMTS surgery is as described in previous studies (*15*). Briefly, 8-weeks-old male mice were anesthetized by ketamine and xylazine. Above the calcaneus, a small incision in the longitudinal axis of the tendon is made in the middle of the tendon. The Achilles tendon is transected in this incision. Sham operations were done on independent mice. For inhibitor treatment experiments, a dose of AMD3100 (10 mg/kg; R&D Systems) and EHT1864 (10 mg/kg; R&D Systems) were administered intraperitoneally twice a week after the PG injection, caged together, or after SMTS surgery.

At the end of each experimental time point, mice were euthanized. Pine specimens of PGIS mice and both hind paws of DBA/1 mice and SMTS mice were dissected and fixed in 4% paraformaldehyde for μCT and histological analyses.

DBA/1-GFP mice parabiosis

C57BL/6-Tg (CAG-EGFP)1Osb/J (GFP mice) were purchased from Charles River Laboratories. A long skin incision was made in GFP and DBA/1 (caged together for 16 to 20 weeks) mice, from the elbow joint along the lateral midline of the body to the knee joint. An incision of about 15 mm was made in the muscle layer, and the muscle incisions of the two mice were anastomosed with 6-0 absorbable silk sutures. GFP and DBA/1 mice were surgically joined together using 4-0 silk sutures along the skin edges of a full-thickness flank incision at the lateral midline. Pain treatment was performed every 12 hours by subcutaneous injection of buprenorphine (Sigma-Aldrich LLC, Darmstadt, Germany) for 3 days. Pain control was performed 7 days afterward as needed. After 4 weeks of feeding on parabiosis, the two mice were euthanized. The hind paws of DBA/1 mice is dissected and fixed in 4% paraformaldehyde for histological and immunofluorescence analysis.

Cell culture

Human bone marrow stem cells were isolated, purified by using density gradient centrifugation, and cultured as previously described (*14*). The samples were minced and digested with collagenase D (1 mg/ml; Roche). The digested specimens were filtered through a 40-μm nylon filter after overnight incubation at 37°C. hBMSCs were suspended in low-glucose Dulbecco's modified Eagle's medium (DMEM; Gibco) supplemented with 10% fetal bovine serum (FBS; Gibco) and 1% penicillin-streptomycin and cultured in a humidified incubator at 37°C and 5% CO^2.

RNA sequencing and data analysis

Samples collected from surgeries immediately enter the RNA extraction program. Total RNA was isolated with TRIzol (MilliporeSigma) and quantified using NanoDrop ND-1000 (Thermo Fisher Scientific). RNA integrity was assessed by standard denaturing agarose gel electrophoresis. Total RNA was first enriched using the NEBNext Poly(A) mRNA Magnetic Isolation Module. The processed RNA product was used for library construction through the KAPA Stranded RNA-Seq Library Prep Kit (Illumina). The constructed library was tested using Agilent 2100 Bioanalyzer, and the library was lastly quantified by qPCR. The digested products were size-selected by agarose gel electrophoresis, PCR-amplified, and sequenced using Illumina HiSeq 4000 (or other platforms) by Gene Denovo Biotechnology Co.

Data were mapped to the reference genome by TopHat2 (version 2.1.1); then, transcript abundances were quantified by the software RSEM (version 1.2.19). First, a set of reference transcript sequences were generated and preprocessed according to transcripts (in FASTA format) and gene annotation files (in GTF format). Second, reads were realigned to the reference transcripts using Bowtie alignment program, and the resulting alignments

were used to estimate transcript abundances. The transcript expression level was normalized by using fragments per kilobase of transcript per million mapped reads. Values of transcripts from the same gene were merged to obtain reads counts and expression level at gene level. Differentially expressed genes were also identified using the edgeR package (version 3.12.1) (http://r-project.org/) with general linear model and a threshold of fold change >2 and false discovery rate <0.05.

Single-cell RNA sequencing

Ligament specimens were minced finely and digested with collagenase D (3 mg/ml; Roche) and Dispase (4 mg/ml; Sigma-Aldrich) for 2 hours. Then, digested tissues were filtered through a 40-μm nylon filter to remove debris. Cells were collected by centrifugation. For single-cell RNA sequencing, R1 (read 1 primer sequence) is added to the molecules during genomics gel in emulsion (GEM) incubation. P5, P7, a sample index, and R2 (read 2 primer sequence) are added during library construction via end repair, A-tailing, adaptor ligation, and PCR. The final libraries contain the P5 and P7 primers used in Illumina bridge amplification. The Single Cell′ Protocol produces Illumina-ready sequencing libraries. A Single Cell′ Library comprises standard Illumina paired-end constructs that begin and end with P5 and P7. The Single Cell 3′ 16–base pair (bp) 10× barcode and 10-bp unique molecular index (UMI) are encoded in read 1, while read 2 is used to sequence the cDNA fragment. Sample index sequences are incorporated as the i7 index read. Read 1 and read 2 are standard Illumina sequencing primer sites used in paired-end sequencing.

Macrophage isolation

The spleen was perfused with 10 ml of phosphate-buffered saline (PBS) injected into left ventricular before dissection. The spleen was then minced into a homogenous paste with a scalpel on a dish plate and then treated with 1 ml of an enzyme cocktail containing collagenase D (1 mg ml^{-1}; Roche), deoxyribonuclease I (100 μg ml^{-1}; Sigma-Aldrich), and 0Dispase (0.6 U ml^{-1}; Roche) in complete DMEM containing 2% FBS. The dissociated spleen samples were resuspended and applied to a strainer (70 μm). Cell sample was incubated with anti-F4/80 microbeads (Miltenyi Biotec) and loaded onto a magnetic LS column (Miltenyi Biotec) placed in the magnetic field of a MACS separator (Miltenyi Biotec). After washing, the magnetically labeled cells were flushed out by firmly pushing the plunger into the column to get F4/80-positive cells.

Enzyme-linked immunosorbent assay

Serum CXCL12 was measured with an enzyme-linked immunosorbent assay (ELISA) kit (Abcam) in plasma samples. All measurements were done according to the manufacturers' instructions. The sensitivity of ELISA for all proteins was 80 pg/ml.

Measurement of cell migration

A chemotaxis assay of hBMSCs was performed with the Boyden chamber method using a 6.5-mm filter with a pore size of 8.0 μm (Transwell, Corning Labware Products). Briefly, DMEM containing 10% FBS and Cxcl12 (50 ng/ml; R&D Systems) was placed as a chemoattractant in the lower wells, and hBMSCs were suspended at a final concentration of 1×10^5 cells/ml in serum-free DMEM in the upper wells. The plate was incubated at 37°C in 5% CO^2 for 12 hours. After incubation, the nonmigrating cells were removed from the filter's upper surface using a cotton swab. The filters were fixed in methanol for 15 min and stained with 0.1% crystal violet for 15 min. Chemotaxis was quantified using an optical microscope to count the stained cells that had migrated to the lower side of the filter. The plate was incubated at 37°C in 5% CO^2 for 24 hours.

Immunofluorescence staining

hBMSCs were seeded in a six-well plate at a density of 2×10^5 cells per well and cultured for 24 hours. The cells were untreated or treated with Cxcl12 (50 ng/ml; R&D Systems) for 24 hours. After being fixed in 4% paraformaldehyde for 15 min and washed with PBS, hBMSCs cells were permeabilized with 0.2% Triton X-100 in PBS (containing 5 mM EDTA and 2% FBS) for 10 min. Washed with PBS, cells were with 2×10^7 M fluorescein isothiocyanate–conjugated phalloidin at room temperature for 1 hour and investigated under a confocal microscope.

μCT analysis

Lumbar spine (spinal segment including intervertebral disc and adjacent end plates) and hind paw specimens were obtained from mice postmortem and fixed with 4% paraformaldehyde. For μCT scanning, specimens were fitted in a cylindrical sample holder and scanned using a Inveon positron emission tomography/CT scanner (Siemens) set to 80 kVp and 450 μA. For visualization, the segmented data were imported and reconstructed as three-dimensional images using Inveon Research Workplace (Siemens, version 4.2.0.8).

Histology and morphometric analysis

Specimens after μCT analysis were fixed in 5% paraformaldehyde solution for 24 hours. The fixed specimens were then decalcified in 10% EDTA (pH 7.0) for 7 days and embedded in paraffin. Blocks were sectioned at 4-μm intervals using a paraffin microtome. About 20 sections being compared were taken at the same anatomical level to ensure that the following experiments were conducted on serial sections and stained. All slides were dewaxed in xylene. Paraffin-embedded sections were stained with H&E and Masson's trichrome to evaluate general structures and with Safranin O and Fast Green (SOFG) and toluidine blue to evaluate bone formation.

Immunostaining was performed using a standard protocol. Immunohistochemical analysis of the specimens was conducted using specific antibodies. Antibodies applied to mouse sections include sdf-1 (Abcam, ab9797), sca-1 (R&D Systems, AF1226), GFP (Abcam, ab13970), PRX-1 (Abcam, ab211292), CD45 (Abcam, ab10558), and F4/80 (Abcam, ab6640). For immunohistochemical staining, we subsequently used a horseradish peroxidase–streptavidin detection system (Dako) to detect the immunoactivity. For immunofluorescence staining, we continued to use secondary antibodies conjugated with red fluorescence, incubated the slides, avoiding light, at room temperature for 1 hour, and mounted the slides with VECTASHIELD Antifade Mounting Medium with 4′,6-diamidino-2-phenylindole. The proportion of positive cells per visual field was calculated using the number of positive cells as the numerator and the number of total cells as the denominator.

Statistical analysis

Analyses were performed using SPSS software for Windows version 22.0. All experiment animals were euthanized at different time points. These are no repeated measurements in the same animal. The unpaired Student's *t* test and paired sample *t* test were used to compare

two groups with Shapiro-Wilk test for normality test. One-way analysis of variance (ANOVA) and with Levene's test for homogeneity of variance, followed by the Tukey's post hoc test or Bonferroni post hoc test based on the comparison to be made and the statistical indication of each test, were used. *P* values are recorded in the statistical chart. Sample sizes were incorporated into the text and figure legends, and individual data points from each replicate were depicted as small circles in all figures.

SUPPLEMENTARY MATERIALS

Supplementary material for this article is available at https://science.org/doi/10.1126/sciadv.abl8054

REFERENCES AND NOTES

1. J. D. Taurog, A. Chhabra, R. A. Colbert, Ankylosing spondylitis and axial spondyloarthritis. *N. Engl. J. Med.* **374**, 2563–2574 (2016).
2. J. Sieper, D. Poddubnyy, Axial spondyloarthritis. *Lancet* **390**, 73–84 (2017).
3. W. Lee, J. D. Reveille, M. H. Weisman, Women with ankylosing spondylitis: A review. *Arthritis Rheum.* **59**, 449–454 (2008).
4. M. M. Ward, A. Deodhar, L. S. Gensler, M. Dubreuil, D. Yu, M. A. Khan, N. Haroon, D. Borenstein, R. Wang, A. Biehl, M. A. Fang, G. Louie, V. Majithia, B. Ng, R. Bigham, M. Pianin, A. A. Shah, N. Sullivan, M. Turgunbaev, J. Oristaglio, A. Turner, W. P. Maksymowych, L. Caplan, 2019 update of the American College of Rheumatology/Spondylitis Association of America/Spondyloarthritis Research and Treatment Network recommendations for the treatment of ankylosing spondylitis and nonradiographic axial spondyloarthritis. *Arthritis Rheumatol.* **71**, 1599–1613 (2019).
5. G. Schett, R. J. Lories, M.-A. D'Agostino, D. Elewaut, B. Kirkham, E. R. Soriano, D. McGonagle, Enthesitis: From pathophysiology to treatment. *Nat. Rev. Rheumatol.* **13**, 731–741 (2017).
6. D. van der Heijde, R. Landewé, Inhibition of spinal bone formation in AS: 10 years after comparing adalimumab to OASIS. *Arthritis Res. Ther.* **21**, 225 (2019).
7. X. Baraliakos, J. Braun, A. Deodhar, D. Poddubnyy, A. Kivitz, H. Tahir, F. van den Bosch, E.-M. Delicha, Z. Talloczy, A. Fierlinger, Long-term efficacy and safety of secukinumab 150 mg in ankylosing spondylitis: 5-year results from the phase III MEASURE 1 extension study. *RMD Open* **5**, e001005 (2019).
8. D. van der Heijde, I.-H. Song, A. L. Pangan, A. Deodhar, F. van den Bosch, W. P. Maksymowych, T.-H. Kim, M. Kishimoto, A. Everding, Y. Sui, X. Wang, A. D. Chu, J. Sieper, Efficacy and safety of upadacitinib in patients with active ankylosing spondylitis (SELECT-AXIS 1): A multicentre, randomised, double-blind, placebo-controlled, phase 2/3 trial. *Lancet* **394**, 2108–2117 (2019).
9. D. Poddubnyy, J. Sieper, Diagnostic delay in axial spondyloarthritis—A past or current problem? *Curr. Opin. Rheumatol.* **33**, 307–312 (2021).
10. M. Van Mechelen, R. Lories, Tenascin-C, a novel target to inhibit new bone formation in axial spondyloarthritis, linked with inflammation, mechanical strain and tissue damage. *Ann. Rheum. Dis.* **80**, 823–824 (2021).
11. E. Gracey, A. Burssens, I. Cambré, G. Schett, R. Lories, I. B. McInnes, H. Asahara, D. Elewaut, Tendon and ligament mechanical loading in the pathogenesis of inflammatory arthritis. *Nat. Rev. Rheumatol.* **16**, 193–207 (2020).
12. E. M. Gravallese, G. Schett, Effects of the IL-23-IL-17 pathway on bone in spondyloarthritis. *Nat. Rev. Rheumatol.* **14**, 631–640 (2018).
13. X. Li, S. Chen, Z. Hu, D. Chen, J. Wang, Z. Li, Z. Li, H. Cui, G. Dai, L. Liu, H. Wang, K. Zhang, Z. Zheng, Z. Zhan, H. Liu, Aberrant upregulation of CaSR promotes pathological new bone formation in ankylosing spondylitis. *EMBO Mol. Med.* **12**, e12109 (2020).
14. X. Li, J. Wang, Z. Zhan, S. Li, Z. Zheng, T. Wang, K. Zhang, H. Pan, Z. Li, N. Zhang, H. Liu, Inflammation intensity-dependent expression of osteoinductive wnt proteins is critical for ectopic new bone formation in ankylosing spondylitis. *Arthritis Rheumatol.* **70**, 1056–1070 (2018).
15. Z. Li, S. Chen, H. Cui, X. Li, D. Chen, W. Hao, J. Wang, Z. Li, Z. Zheng, Z. Zhang, H. Liu, Tenascin-C-mediated suppression of extracellular matrix adhesion force promotes entheseal new bone formation through activation of Hippo signalling in ankylosing spondylitis. *Ann. Rheum. Dis.* **80**, 891–902 (2021).
16. C. H. Liu, S. Raj, C.-H. Chen, K.-H. Hung, C.-T. Chou, I.-H. Chen, J.-T. Chien, I.-Y. Lin, S.-Y. Yang, T. Angata, W.-C. Tsai, J. C.-C. Wei, I.-S. Tzeng, S.-C. Hung, K.-I. Lin, HLA-B27-mediated activation of TNAP phosphatase promotes pathogenic syndesmophyte formation in ankylosing spondylitis. *J. Clin. Invest.* **129**, 5357–5373 (2019).
17. J. M. Berthelot, B. Le Goff, Y. Maugars, Bone marrow mesenchymal stem cells in rheumatoid arthritis, spondyloarthritis, and ankylosing spondylitis: Problems rather than solutions? *Arthritis Res. Ther.* **21**, 239 (2019).
18. X. Shen, Y. Zhang, Y. Gu, Y. Xu, Y. Liu, B. Li, L. Chen, Sequential and sustained release of SDF-1 and BMP-2 from silk fibroin-nanohydroxyapatite scaffold for the enhancement of bone regeneration. *Biomaterials* **106**, 205–216 (2016).
19. H. Zhang, S. Yu, X. Zhao, Z. Mao, C. Gao, Stromal cell-derived factor-1α-encapsulated albumin/heparin nanoparticles for induced stem cell migration and intervertebral disc regeneration in vivo. *Acta Biomater.* **72**, 217–227 (2018).
20. R. Janssens, S. Struyf, P. Proost, The unique structural and functional features of CXCL12. *Cell. Mol. Immunol.* **15**, 299–311 (2018).
21. R. Bragg, W. Gilbert, A. M. Elmansi, C. M. Isales, M. W. Hamrick, W. D. Hill, S. Fulzele, Stromal cell-derived factor-1 as a potential therapeutic target for osteoarthritis and rheumatoid arthritis. *Ther. Adv. Chronic Dis.* **10**, 204062231988253 (2019).
22. P. F. Chen, J. Tao, S. Zhu, Y. Cai, Q. Mao, D. Yu, J. Dai, H. W. Ouyang, Radially oriented collagen scaffold with SDF-1 promotes osteochondral repair by facilitating cell homing. *Biomaterials* **39**, 114–123 (2015).
23. R. Holmdahl, L. Jansson, M. Andersson, R. Jonsson, Genetic, hormonal and behavioural influence on spontaneously developing arthritis in normal mice. *Clin. Exp. Immunol.* **88**, 467–472 (1992).
24. R. J. U. Lories, I. Derese, F. P. Luyten, Modulation of bone morphogenetic protein signaling inhibits the onset and progression of ankylosing enthesitis. *J. Clin. Invest.* **115**, 1571–1579 (2005).
25. S. E. Berlo, T. Guichelaar, C. B. ten Brink, P. J. van Kooten, F. Hauet-Broeren, K. Ludanyi, W. van Eden, C. P. Broeren, T. T. Glant, Increased arthritis susceptibility in cartilage proteoglycan-specific T cell receptor-transgenic mice. *Arthritis Rheum.* **54**, 2423–2433 (2006).
26. R. A. Bartolomé, I. Molina-Ortiz, R. Samaniego, P. Sánchez-Mateos, X. R. Bustelo, J. Teixidó, Activation of Vav/Rho GTPase signaling by CXCL12 controls membrane-type matrix metalloproteinase-dependent melanoma cell invasion. *Cancer Res.* **66**, 248–258 (2006).
27. H. Fleige, S. Ravens, G. L. Moschovakis, J. Bölter, S. Willenzon, G. Sutter, S. Häussler, U. Kalinke, I. Prinz, R. Förster, IL-17-induced CXCL12 recruits B cells and induces follicle formation in BALT in the absence of differentiated FDCs. *J. Exp. Med.* **211**, 643–651 (2014).
28. V. Ranganathan, E. Gracey, M. A. Brown, R. D. Inman, N. Haroon, Pathogenesis of ankylosing spondylitis—Recent advances and future directions. *Nat. Rev. Rheumatol.* **13**, 359–367 (2017).
29. A. A. El-Zayadi, E. A. Jones, S. M. Churchman, T. G. Baboolal, R. J. Cuthbert, J. J. El-Jawhari, A. M. Badawy, A. A. Alase, Y. M. El-Sherbiny, D. M. Gonagle, Interleukin-22 drives the proliferation, migration and osteogenic differentiation of mesenchymal stem cells: A novel cytokine that could contribute to new bone formation in spondyloarthropathies. *Rheumatology (Oxford)* **56**, 488–493 (2017).
30. M. Benjamin, H. Toumi, D. Suzuki, S. Redman, P. Emery, D. McGonagle, Microdamage and altered vascularity at the enthesis-bone interface provides an anatomic explanation for bone involvement in the HLA-B27-associated spondylarthritides and allied disorders. *Arthritis Rheum.* **56**, 224–233 (2007).
31. M. Machacek, L. Hodgson, C. Welch, H. Elliott, O. Pertz, P. Nalbant, A. Abell, G. L. Johnson, K. M. Hahn, G. Danuser, Coordination of Rho GTPase activities during cell protrusion. *Nature* **461**, 99–103 (2009).
32. B. A. Teicher, S. P. Fricker, CXCL12 (SDF-1)/CXCR4 pathway in cancer. *Clin. Cancer Res.* **16**, 2927–2931 (2010).
33. R. Lories, The balance of tissue repair and remodeling in chronic arthritis. *Nat. Rev. Rheumatol.* **7**, 700–707 (2011).
34. P. Ajrawat, Z. Touma, I. Sari, C. Taheri, J. P. Diaz Martinez, N. Haroon, Effect of TNF-inhibitor therapy on spinal structural progression in ankylosing spondylitis patients: A systematic review and meta-analysis. *Int. J. Rheum. Dis.* **23**, 728–743 (2020).
35. M. H. Kaaij, M. N. van Tok, I. C. Blijdorp, C. A. Ambarus, M. Stock, D. Pots, V. L. Knaup, M. Armaka, E. Christodoulou-Vafeiadou, T. K. van Melsen, H. Masdar, H. J. P. P. Eskes, N. G. Yeremenko, G. Kollias, G. Schett, S. W. Tas, L. M. van Duivenvoorde, D. L. P. Baeten, Transmembrane TNF drives osteoproliferative joint inflammation reminiscent of human spondyloarthritis. *J. Exp. Med.* **217**, (2020).
36. M. N. van Tok, L. M. van Duivenvoorde, I. Kramer, P. Ingold, S. Pfister, L. Roth, I. C. Blijdorp, M. G. H. van de Sande, J. D. Taurog, F. Kolbinger, D. L. Baeten, Interleukin-17A inhibition diminishes inflammation and new bone formation in experimental spondyloarthritis. *Arthritis Rheumatol.* **71**, 612–625 (2019).
37. L. M. van Duivenvoorde, M. L. Dorris, N. Satumtira, M. N. van Tok, K. Redlich, P. P. Tak, J. D. Taurog, D. L. Baeten, Relationship between inflammation, bone destruction, and osteoproliferation in the HLA-B27/human β2-microglobulin-transgenic rat model of spondylarthritis. *Arthritis Rheum.* **64**, 3210–3219 (2012).
38. P. Jacques, S. Lambrecht, E. Verheugen, E. Pauwels, G. Kollias, M. Armaka, M. Verhoye, A. van der Linden, R. Achten, R. J. Lories, D. Elewaut, Proof of concept: Enthesitis and new bone formation in spondyloarthritis are driven by mechanical strain and stromal cells. *Ann. Rheum. Dis.* **73**, 437–445 (2014).
39. E. Vieira-Sousa, L. M. van Duivenvoorde, J. E. Fonseca, R. J. Lories, D. L. Baeten, Review: Animal models as a tool to dissect pivotal pathways driving spondyloarthritis. *Arthritis Rheumatol.* **67**, 2813–2827 (2015).
40. V. A. Adarichev, T. T. Glant, Experimental spondyloarthropathies: Animal models of ankylosing spondylitis. *Curr. Rheumatol. Rep.* **8**, 267–274 (2006).

41. T. Bardos, Z. Szabo, M. Czipri, C. Vermes, M. Tunyogi-Csapo, R. Urban, K. Mikecz, T. Glant, A longitudinal study on an autoimmune murine model of ankylosing spondylitis. *Ann. Rheum. Dis.* **64**, 981–987 (2005).
42. A. Hanyecz, S. E. Berlo, S. Szántó, C. P. M. Broeren, K. Mikecz, T. T. Glant, Achievement of a synergistic adjuvant effect on arthritis induction by activation of innate immunity and forcing the immune response toward the Th1 phenotype. *Arthritis Rheum.* **50**, 1665–1676 (2004).
43. X. Wang, L. Xie, J. Crane, G. Zhen, F. Li, P. Yang, M. Gao, R. Deng, Y. Wang, X. Jia, C. Fan, M. Wan, X. Cao, Aberrant TGF-β activation in bone tendon insertion induces enthesopathy-like disease. *J. Clin. Invest.* **128**, 846–860 (2018).
44. B. Bockorny, V. Semenisty, T. Macarulla, E. Borazanci, B. M. Wolpin, S. M. Stemmer, T. Golan, R. Geva, M. J. Borad, K. S. Pedersen, J. O. Park, R. A. Ramirez, D. G. Abad, J. Feliu, A. Muñoz, M. Ponz-Sarvise, A. Peled, T. M. Lustig, O. Bohana-Kashtan, S. M. Shaw, E. Sorani, M. Chaney, S. Kadosh, A. Vainstein Haras, D. D. von Hoff, M. Hidalgo, BL-8040, a CXCR4 antagonist, in combination with pembrolizumab and chemotherapy for pancreatic cancer: The COMBAT trial. *Nat. Med.* **26**, 878–885 (2020).
45. J. Wang, B. A. Tannous, M. C. Poznansky, H. Chen, CXCR4 antagonist AMD3100 (plerixafor): From an impurity to a therapeutic agent. *Pharmacol. Res.* **159**, 105010 (2020).
46. I. M. Ghobrial, C.-J. Liu, R. A. Redd, R. P. Perez, R. Baz, O. Zavidij, R. Sklavenitis-Pistofidis, P. G. Richardson, K. C. Anderson, J. Laubach, P. Henrick, A. Savell, K. Reyes, K. Hornburg, S. Chuma, P. Sabbatini, M. D. Robbins, P. S. Becker, A phase Ib/II trial of the first-in-class anti-CXCR4 antibody ulocuplumab in combination with lenalidomide or bortezomib plus dexamethasone in relapsed multiple myeloma. *Clin. Cancer Res.* **26**, 344–353 (2020).

Acknowledgments
Funding: This work was supported by National Natural Science Foundation of China (grant nos. 81972039 and 81772307), Science and Technology Planning Project of Guangdong Province, China (grant nos. 2017A050501016), Special Support Plan for High-Level Talent of Guangdong Province, China (grant no. 2016TQ03R667), the Natural Science Foundation of Guangdong province (grant no. S2013010015397), Natural Science Foundation of Guangdong Province-Outstanding Youth project (2021B1515020080), and KELIN New Talent Project of The First Affiliated Hospital, Sun Yat-sen University (grant no. Y12001). **Author contributions:** H.L. conceived the ideas for experimental designs. H.C., Zihao Li, and S.C. conducted most of the experiments, analyzed data, and prepared the manuscript. D.C. and Z.Zha. conducted sample collection and performed statistical analysis. X.L., J.W., Zemin Li, and Z.Zhe. provided critical suggestions and instructions for the project and helped compose the manuscript. H.C. provided μCT analysis. H.C., W.H., F.Z., and K.Z. conducted most animal experiments and performed analysis. H.L. developed the concept, supervised the project, and conducted data analysis. **Competing interests:** The authors declare that they have no competing interests. **Data and materials availability:** All data needed to evaluate the conclusions in the paper are present in the paper and/or the Supplementary Materials.

Submitted 6 August 2021
Accepted 15 February 2022
Published 6 April 2022
10.1126/sciadv.abl8054